Influence of Nozzle Diameter on Electric Arc Dynamics and Coating Properties in a Cascaded-Anode Plasma Torch

Céline Ruelle, Simon Goutier, Vincent Rat, Geoffroy Rivaud, Alan Kéromnès, Christophe Chazelas, Érick Meillot

Influence of Nozzle Diameter on Electric Arc Dynamics and Coating Properties in a Cascaded-Anode Plasma Torch

Céline RUELLE[1], Simon GOUTIER[1], Vincent RAT[1], Geoffroy RIVAUD[1], Alan KÉROMNÈS[1], Christophe CHAZELAS[1], Érick MEILLOT[2]

[1]Univ. Limoges, CNRS, IRCER UMR 7315, F-87000 Limoges, France
[2]CEA, DAM, Le Ripault, F-37260 Monts, France

Corresponding author:

Céline RUELLE
IRCER
12 rue Atlantis 87068 Limoges, France
+33587502413

Abstract

Electric arc dynamics in plasma torches have an influence of the plasma jet stability and could impact coating properties. Depending on the plasma torch design, voltage fluctuations may vary from a hundred to only a few percent of the mean voltage. A cascaded-anode plasma torch particularly leads to very low voltage fluctuation, due to the presence of neutrodes limiting the amplitude of arc fluctuations. However, the electric arc dynamics and electrode erosion process are still poorly understood in this kind of plasma torches. The aim of this work is to refine the knowledge on the influence of the nozzle's diameter on electric arc dynamics and on zirconia-yttria coating properties. Two plasma-forming gas compositions were studied, connecting several analysis methods (end-on imaging, current and voltage time monitoring, plasma light fluctuations at nozzle exit, thermal balance evaluation and in-flight particles assessment) to coatings characterization (porosity and hardness measurements). Reducing the nozzle's diameter from 9 to 6.5 mm results in higher voltage fluctuations and thermal efficiency of the plasma torch. This is due to the warm plasma gas being more evenly distributed in the anode nozzle. After testing, surveys of the 6.5 mm in diameter nozzle show significant longitudinal wear, which may highlight an axial movement of the electric arc on the anode's surface, leading to high voltage fluctuations. Finally, the particle velocity is higher in a 6.5 mm in diameter nozzle, resulting in a lower particle temperature and a higher coating porosity.

Introduction

Thermal spraying processes are widely used in several industrial sectors, including the aeronautical and automotive industries (Ref 1). This technology may require the use of a non-transferred-arc plasma torch, which is made up of a rod-shaped tungsten cathode with a conical tip and of a coaxial water-cooled copper anode, also used as a nozzle. A plasma-forming gas is injected in the cathode cavity and a high-current arc is generated between the two electrodes. The energy discharged in the electric arc enables the ionization of the plasma gas, resulting in the creation of a plasma jet. Particles are then injected into this high specific enthalpy medium, where they will be melted and sprayed towards the workpiece to be coated. The characteristics of the injected particles (temperature and velocity) depend on the plasma jet fluctuations which are influenced by the electric arc dynamics. The anodic arc attachment is subject to the hydrodynamic and Lorentz forces in particular, leading to arc voltage fluctuations. In the case of conventional plasma torches with a large anodic surface (such as F4 plasma torches, Fig. 1 A), instabilities can be significant and are categorized into several modes including steady, restrike, take-over or Helmholtz modes (Ref 2–7). The steady mode corresponds to a fixed location of the arc root on the anode's surface, with an electric arc voltage considered to be constant (voltage fluctuations are negligible). The restrike mode exhibits a saw-tooth shaped voltage signal. It corresponds to a fast process which creates a new arc attachment at the anode wall due to the breakdown of the cold boundary layer around the arc column following an arc elongation. As for the take-over mode, a sinusoidal voltage signal is observed, related to the back-and-forth movement of the arc root along the anode's surface. In the Helmholtz mode, due to the torch design, a coupling between pressure in the torch and voltage brings about a significant mass flow rate modulation that affects the arc column. Depending on the plasma spraying conditions, a combination of several modes of instabilities can be observed. These different dynamics for the arc root were highlighted through the synchronization of fast photography and arc voltage measurements by Ghorui *et al*. (Ref 8).

In order to reduce these instabilities, improvements have been applied to plasma torch design. For instance, cascaded-anode plasma torches were developed to limit the arc root's movement on the anode's surface. An additional stage called "neutrode stacking" (each neutrode is at an electrically floating potential) is also carried out between the two electrodes, as well as the implementation of a reduced anodic surface. This configuration shows lower voltage fluctuations and an increase in the arc's length, which results in a higher arc voltage. There are three types of cascaded-anode plasma torches: plasma torches with three cathodes and a single cascaded-anode (such as the TriplexPro™ from Oerlikon Metco, Westbury NY, U.S.A), plasma torches with a single cathode and three cascaded-anodes (such as the Delta Gun from GTV GmbH, Luckenbach, Germany) (Ref 9) and plasma torches with a single cathode and a single cascaded-anode (such as the SinplexPro™ from Oerlikon Metco). A simplified schematic with the meaningful dimensions of a SinplexPro™ plasma torch with a 9 mm in diameter nozzle is presented in Fig. 1 B.

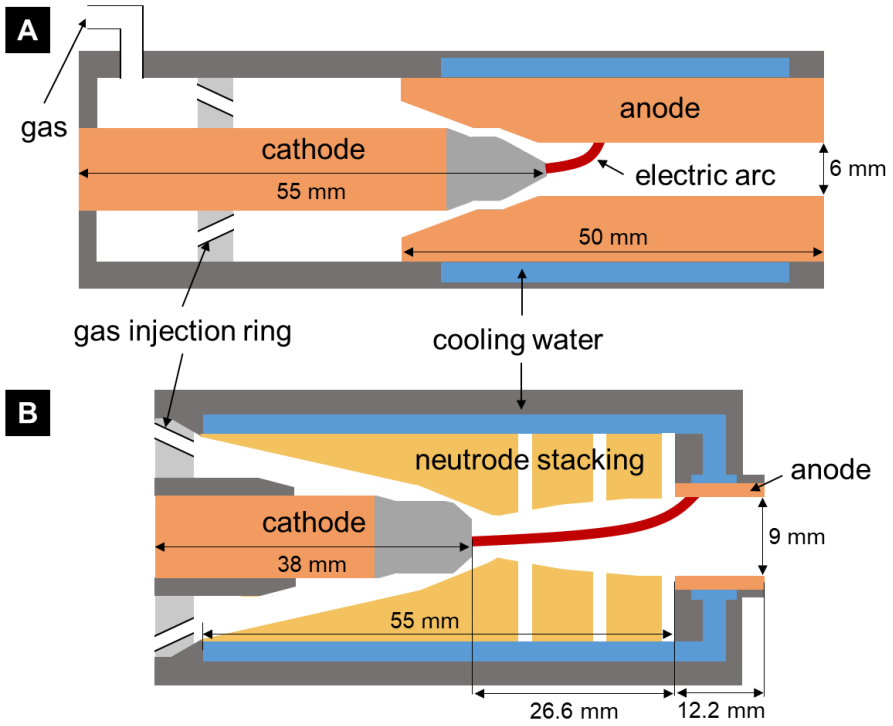

Figure 1: Schematic with the meaningful dimensions of A) a F4 (conventional plasma torch) and B) a SinplexPro™ (cascaded-anode plasma torch). Adapted from (Ref 10).

A plasma torch behavior depends on numerous parameters, including the current, the plasma forming gases composition, the flow rates. The torch design also is of high importance since the nozzle diameter or the neutrode arrangement for cascaded-anode torches directly affect the plasma jet properties. For instance, Coudert *et al.* and Planche *et al*. (Ref 11,12) showed that reducing the nozzle diameter in a conventional plasma torch operating following a pure restrike mode for the same plasma gas composition (Ar-H_2 45-15 slpm) results in reduced jumps in voltage amplitude and higher mean voltages due to arc column constriction. (Ref 13) features a comparison between a SinplexPro™ and a F4 for the same plasma-forming gas composition. In the cascaded-anode plasma torch, mean voltages are higher and voltage fluctuations are reduced, while in a F4 conventional plasma torches the voltage fluctuations amplitude is about 75 V. Furthermore, for cascaded-anode plasma torch, the number of neutrode stacks will define the distance between the cathode tip and the anode, resulting in different arc lengths. Darut *et al*. (Ref 14) studied the effects of the number of neutrodes on the voltage fluctuations and on the quality of the coatings, eventually comparing the results to a F4 conventional plasma torch. They highlighted a higher arc stability with a cascaded-anode plasma torch, and this regardless of the number of neutrodes (max. 16 % of voltage fluctuations compared to the 97 % observed with a conventional plasma torch). However, although similar coating properties were achieved with the two geometries of plasma torches, the cascaded-anode plasma torch was operating at a lower current value with a lower amount of hydrogen. Since these two parameters are critical regarding electrode erosion and power consumption, a cascaded-anode plasma torch is a promising tool for the industry. The influence of the distance between the cathode tip and the nozzle on the plasma jet characteristics was also studied with a laminar plasma torch working with pure N_2, as displayed in (Ref 15). The authors showed than increasing this distance results in a higher mean voltage, a higher specific enthalpy and a higher plasma jet length.

As explained above, the benefits of a cascaded-anode plasma torch have been referenced by means of higher electric arc stability and higher electrical power, but the question of anode erosion is still remaining since it is directly linked to the arc root attachment on the anode's

surface. Anode erosion will not only affect the electrode's lifespan, but also the quality of the coating, as shown by Leblanc *et al*. in (Ref 16) with a conventional plasma torch. They noticed a significant decrease in temperature and velocity of the injected particles after several hours of operating, resulting in a higher coating porosity rate. One way of controlling the movement of the anodic arc root and reducing anode erosion is to apply an external magnetic field, as suggested in (Ref 17,18), to a cascaded-anode plasma torch.

Therefore, studying the electric arc dynamics in a cascaded-anode plasma torch is a crucial step in the understanding of the behavior of plasma torches and of the anode erosion phenomena. It appears an experimental study relying on the electric arc observation inside the anode nozzle is missing in order to better understand the behavior of cascaded-anode plasma torches. The aim of this study is thus to highlight the influence of the nozzle's diameter on electric arc dynamics and coating properties for two different plasma-forming gas compositions in a cascaded-anode plasma torch.

The experimental conditions selected for this study, namely two different plasma-forming gas compositions and two different diameters for the nozzle, are presented in the first section, whereas a description of the analysis methods used is available afterwards. Anodic arc root observations for different experimental conditions are introduced and discussed in the subsequent section, including the influence of the nozzle's diameter and the gas composition on the injected particle temperature and velocity as well as on and coatings properties. In the last section, conclusion is given.

Experimental set-up & Materials

The plasma torch used for this experiment is the SinplexPro^{TM} from Oerlikon Metco (Westbury NY, U.S.A.), which as a 3-neutrodes stack cascaded-anode geometry, and is studied with two nozzles of 9 and 6.5 mm in diameter. A schematic of the experimental setup is displayed in Fig. 2.

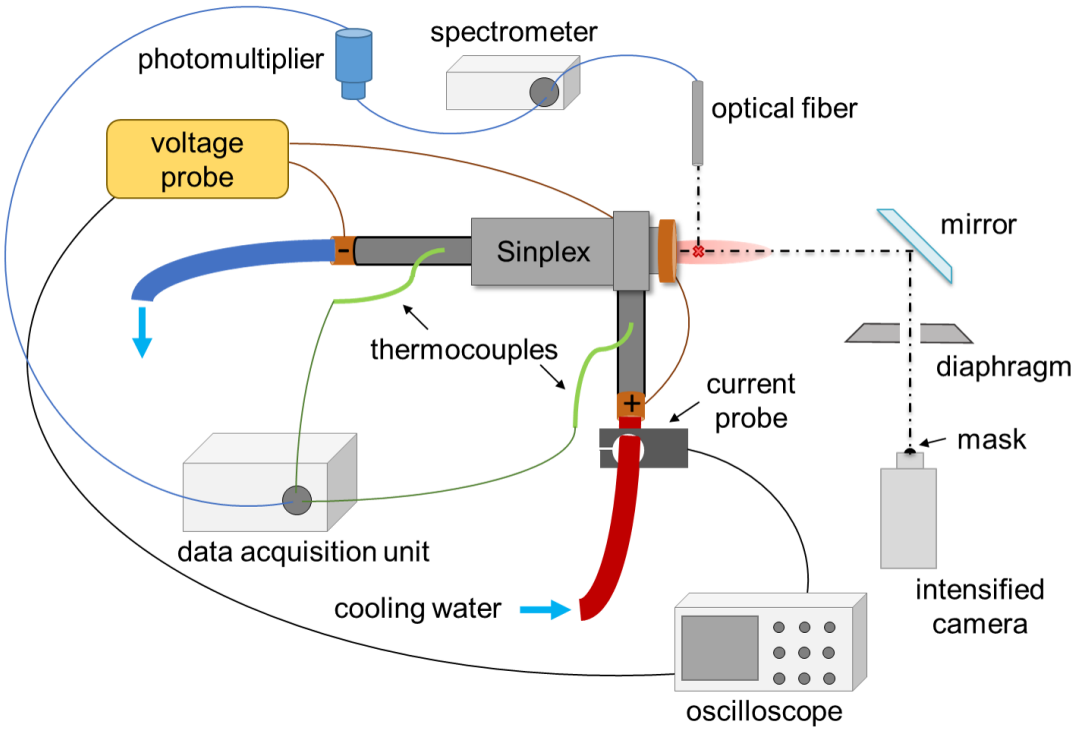

Figure 2: Schematic of the different analysis devices used to characterize the SinplexPro™ plasma torch, allowing measuring and recording thermal balances, arc voltage and current fluctuations, anodic arc root motion and plasma jet light fluctuations. Adapted from (Ref 10).

A mirror and an intensified 16-bit camera (Model pco.dicam C1 by PCO Imaging, Germany) equipped with a Questar QM1 lens were used for imaging the arc attachment inside the anode. Plasma core radiative emissions are much higher than plasma emissions at the anode wall, as shown in Fig. 3 which presents the temperature profile calculated at the nozzle exit from a transient, 3D and non-equilibrium model of SinplexPro™ torch (Ref 19). The plasma-forming gas, the nozzle diameter and the arc current were respectively 60 slpm of argon, 9 mm and 500 A. The net emission coefficient profile of pure argon at Local Thermodynamic Equilibrium (LTE) is also pointed out in Fig. 3 and comes from (Ref 19). Four orders of magnitude in the radiation emission between the axis (r = 0 mm) and the anode wall (r = 4.5 mm) may be highlighted. As the light emitted from the high-temperature column is very intense and interferes with the observations of the arc attachment, a mask is required in order to avoid camera saturation and thus successfully study the arc root's shape and location.

An intensified camera provides 16-bit images in grey scale, meaning that each pixel corresponds to a value ranging from 0 (black) to 65,535 (white). According to Fig. 3, the emission coefficient is approximately 10^5 W.m^{-3} at the anode wall, and is attributed to the lowest value of brightness (0), whereas the highest value of brightness (65,535) may be set at 6.55×10^9 W.m^{-3}. Additionally, as a shade 8 optical filter with a transmittance of 10 % in the visible spectral range was used to reduce the light signal, the maximum brightness should not exceed 6.55×10^8 W.m^{-3}.

As shown in Fig. 3, this emission coefficient value corresponds to a radius of about 3 mm. Thus, for all plasma-forming gas compositions, a mask with a radius of 3 mm was applied for a nozzle of 9 mm in diameter, while being reduced to about 2.6 mm for a 6.5 mm one.

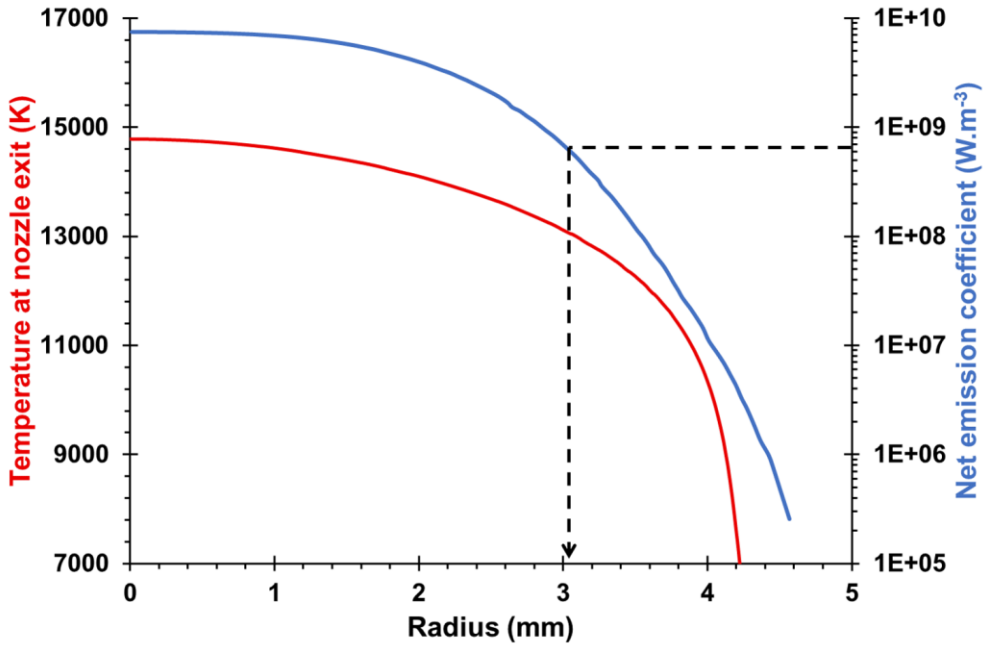

Figure 3: Simulated temperature profile at the nozzle's exit and net emission coefficient profile from (Ref 19) for pure argon at 500 A with a nozzle of 9 mm in diameter.

The frame rate of the intensified camera was set to 120 frames per second with 60 ns of exposure time. Figure 4 displays an example of the type of image gathered. It is to be noted that grey scale images were transformed into in pseudo-colored images according to a lookup table available in the ImageJ software in order to facilitate the arc root visualization. The intensity of pseudo-colored images can be compared, as differences in color are related to the differences in intensity of the original image. In Fig. 4 B, the orange ring represents the nozzle's

surface and the yellow ring delineates the mask. Image analyses were then carried out at the dashed line of interest represented in white in Fig. 4 B, consisting of a 720-point circle (one point every 0.5 °). The light intensity is thus measured at each point along the line of interest, and the data collected may be used to create a radar diagram (with light intensity represented as a function of the angle), which is meaningful to highlight anodic arc roots.

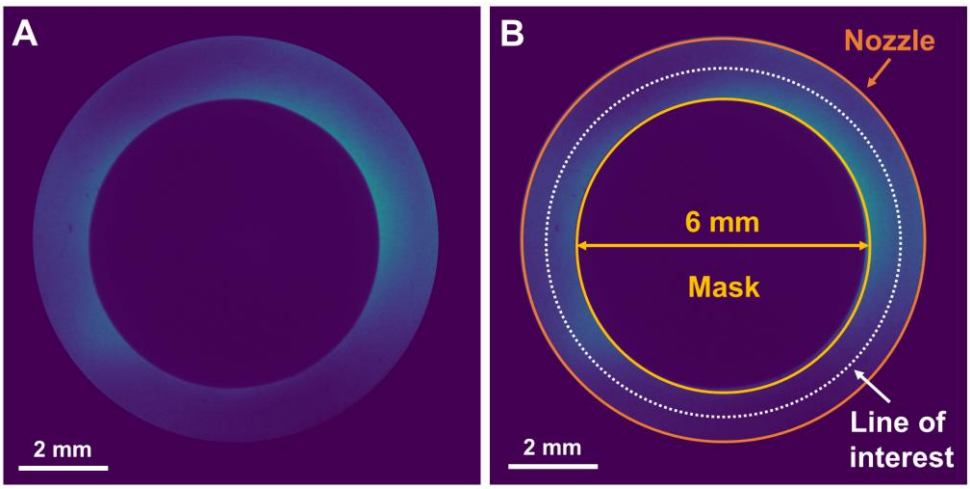

Figure 4: A) Example of an image obtained with the intensified camera for the Ar-H_2 mixture at 500 A and B) the nozzle's surface and mask delimitations (in orange and yellow respectively), and the line of interest (white) used for image analysis. The camera exposure time is 60 ns.

A differential probe 1/20 (METRIX MX9030Z, 30 MHz bandwidth, ± 600 V, accuracy ± 3%) was used to measure the mean voltage and voltage fluctuations between the two electrodes. The voltage fluctuations (VF) percentage is defined by $VF = \frac{2\sigma}{\bar{U}}$ (adapted from (Ref 20)) where σ and $\bar{U}$ are the standard deviation and the mean voltage (in V), respectively. The evolution of the arc current was also measured using a current probe LeCroy CP500 (2 MHz bandwidth). The arc current fluctuation (CF) percentage is then defined by $CF = \frac{2\sigma}{\bar{I}}$ where σ and $\bar{I}$ are the standard deviation and the mean current intensity (in A), respectively. In order to study the influence of current fluctuations on voltage signals, both aforementioned measurements were recorded using a WaveSurfer 3024 Teledyne LeCroy oscilloscope (200 MHz bandwidth). Two J-thermocouples were installed to measure the temperature variation ΔT between the inlet and outlet of the torch's water cooling system, thus allowing to quantify Q_{loss} as the heat loss in this system through Equation *(1)*:

$$Q_{loss} = \dot{m}_w c_p \Delta T \quad (1)$$

where $\dot{m}_w$ is the water mass flow rate in kg.s^{-1} and c_p the water specific heat in J.kg^{-1}.K^{-1} ($\dot{m}_w$ = 0.34 kg.s^{-1} and c_p = 4,184 J.kg^{-1}.K^{-1}). Moreover, the thermal efficiency of the plasma torch η and the specific enthalpy h can be derived from Equations *(2)* and *(3)*:

$$\eta = 1 - \frac{Q_{loss}}{\bar{U}I} \quad (2)$$

$$h = \eta \frac{\bar{U}I}{\dot{m}} \quad (3)$$

with $\bar{U}$ and I being respectively the mean arc voltage (in V) and arc current intensity (in A) respectively, and $\dot{m}$ the total gas mass flow rate in kg.s^{-1}.

Lastly, optical emission spectroscopy (HRS 2 Jobin Yvon spectrometer) was operated to follow the light fluctuations of the plasma jet. The Ar I line located at 420 nm was used because of its high relative intensity (Ref 21). The measurements were carried out using an optical fiber placed at 5 mm from the nozzle's exit; the spectrometer filtered the light signal and then sent it to a photomultiplier (R928 Hamamatsu) which converted this light signal into an electrical one.

In order to evaluate the influence of the nozzle's diameter on coating properties, a zirconia-yttria powder (ZrO_2-7wt.%Y_2O_3), with a particle size distribution ranging from 21 to 51 µm, was injected into the plasma plume. In-flight particle characteristics were studied with a SprayWatch 2S device (Oseir Ltd., Tampere, Finland) to assess the average particle temperature and velocity at 120 mm from the torch's exit (Fig. 5 A). The uncertainty on the consequent results (the chart compiling those results is to be found in the last subsection of the Results & Discussion part) matches the standard deviation of the distribution. Coatings were then produced on sand-blasted stainless-steel substrates (with a surface roughness R_a of about 4 µm) at a stand-off distance of 120 mm (Fig. 5 B).

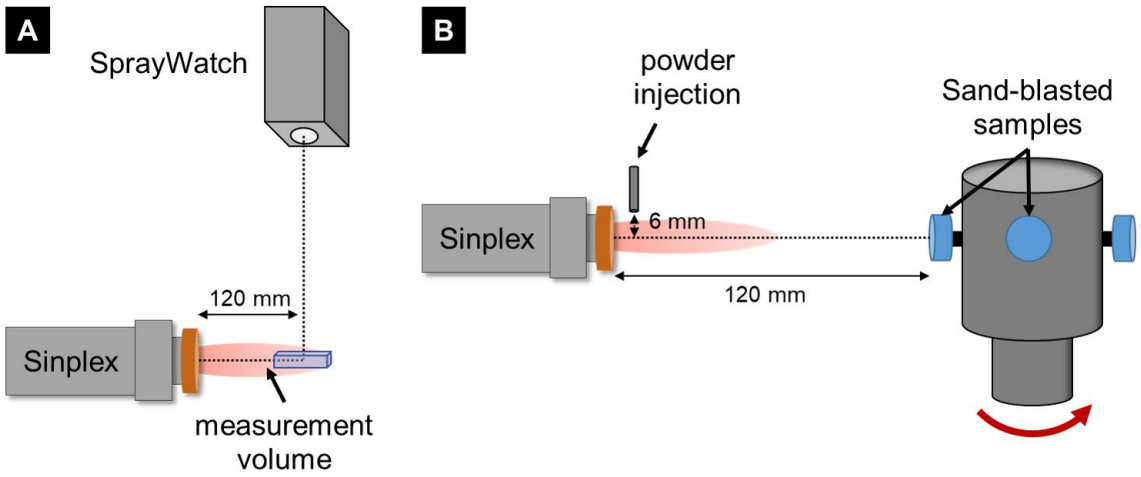

Figure 5: Schematics of A) the SprayWatch measurements and B) the spraying system.

Microhardness measurements were performed on the polished cross-section of the coatings using a Vickers indenter with a load of 0.2 kg. The hardness results shown represent an average of ten measurements with a 200 µm interval for each coating. The uncertainty on these measurements corresponds to the standard deviation of the ten measurements. The ImageJ software was then used to evaluate the average coating porosity by image thresholding applied to five images at a magnification of 1 000.

Two plasma-forming gas compositions were studied: a mixture of argon and hydrogen (Ar-H_2) and a mixture of argon and helium (Ar-He), whose total mass flow rates were nearly the same (1.50 and 1.44 g.s^{-1} for Ar-H_2 and Ar-He respectively). The arc current intensity was set at 500 A for both the 9 and 6.5 mm nozzle. Since time-based analyses are performed in this study, the velocities and residence times for the two different nozzles are gathered in Table 1, which summarizes the experimental conditions implemented as well. The plasma gas velocity has been determined using the equation $v_{gas} = \frac{\dot{m}}{\rho S}$, where $\dot{m}$ is its total mass flow rate (kg.s^{-1}), ρ the plasma gas density (kg.m^{-3}) estimated from the specific enthalpy, and S the nozzle section (m^2). The plasma gas residence time in the nozzle was calculated using $t_{gas} = \frac{l}{v_{gas}}$ with l being the nozzle length (l = 12.2 mm as reported in Fig. 1). It appears that the plasma gas velocity

is higher for the smaller section of the nozzle, as well as for the Ar-He mixture due to its lower density.

Table 1: Experimental conditions implemented, as well as gas velocity and gas residence time for the two nozzle diameters.

Plasma-forming gas	Total mass flow rate ($g.s^{-1}$)	Current (A)	Nozzle diameter (mm)	Gas velocity ($m.s^{-1}$)	Gas residence time (ms)
Ar-H_2	1.50	500	9	715	0.017
			6.5	1190	0.010
Ar-He	1.44		9	1355	0.009
			6.5	2290	0.005

It is to be noted that, in the case of the SinplexPro^{TM}, the manufacturer does not recommend the use of hydrogen with a 6.5 mm nozzle in diameter. However, it is known that this plasma gas is significant for an improved thermal treatment of particles. This study will allow exploring 1) the expansion of the operating scope of this plasma torch and 2) the potential substitution of helium, as it is subject to a risk of shortage.

Results & Discussion

End-on imaging of the arc attachment

Anodic arc root observations were undertaken for both plasma-forming gas compositions and both diameters of the nozzle. Some examples of images captured for each experimental condition are displayed in Fig. 6. Figures 6 A1 and A2 on one hand, and 6 B1 and B2 on the other hand, correspond to the Ar-H_2 and Ar-He mixtures respectively. A radar diagram, generated according to the method described in the experimental set-up section, is displayed next to each composition.

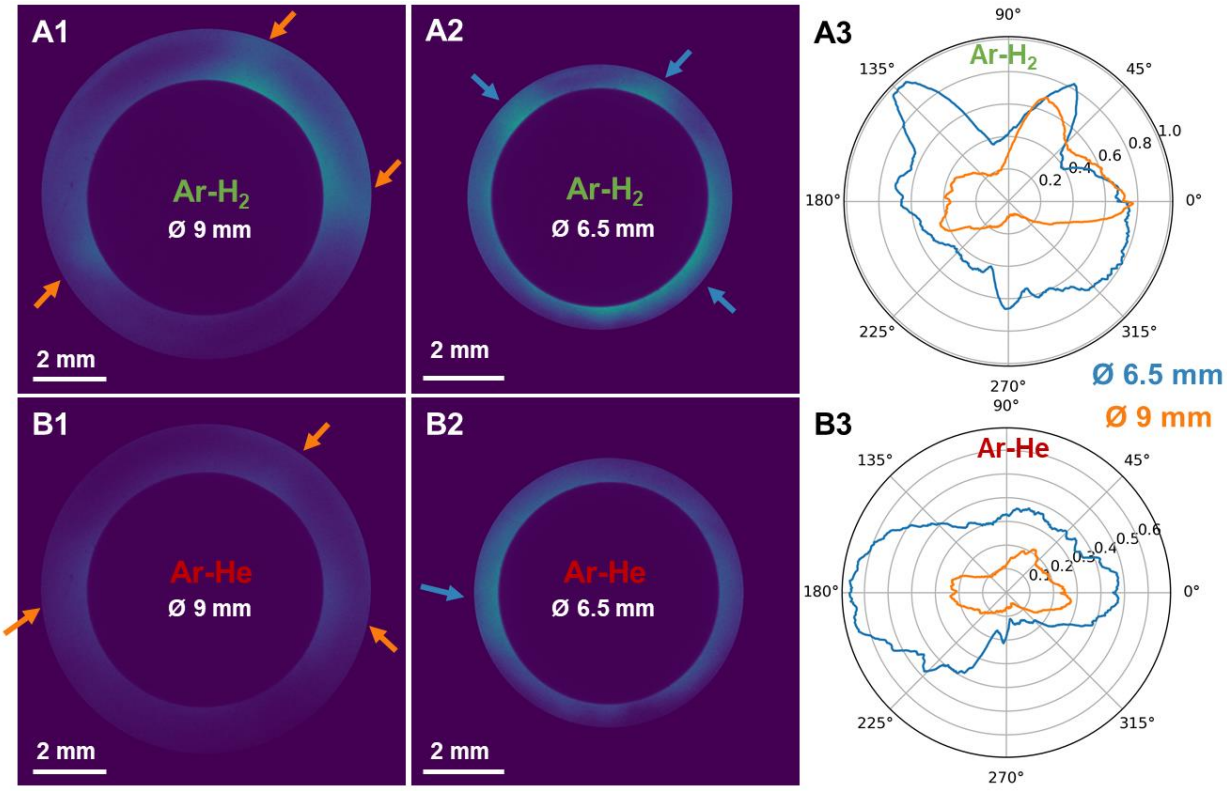

Figure 6: Examples of end-on images obtained for A1) the Ar-H_2 mixture with a 9 mm diameter nozzle, A2) the Ar-H_2 mixture with a 6.5 mm diameter nozzle, B1) the Ar-He mixture with a 9 mm diameter nozzle and B2) the Ar-He mixture with a 6.5 mm diameter nozzle. Orange and blue arrows point arc roots out. The radar diagrams A3) and B3) correspond to the Ar-H_2 and Ar-He mixtures respectively. The camera exposure is time 60 ns.

In the first place, it is worth noting that, regardless of the nozzle's diameter, a more luminous plasma gas is produced with the Ar-H_2 mixture than with the Ar-He one. It suggests higher energy density coming from the dissipation of the electrical power and heat diffusion, which is enhanced in Ar-H_2 due to the H_2 dissociation taking place at low temperature, around 3,500 K (Ref 22). Radial heat diffusion is expected to be higher for this mixture compared with Ar-He mixture, resulting in a warmer cold boundary layer. Moreover, it will be shown below that mean voltage of Ar-H_2 plasma is higher, and can also explain the higher plasma light intensity.

In the case of the Ar-H_2 mixture with a 9 mm nozzle (Fig. 6 A1), three anodic arc roots were clearly visible simultaneously, as pointed out by orange arrows. Figure 7 presents the radar diagrams highlighting movement of these arc roots. It is based on the light intensity measured along the line of interest for three successive images, the first one being taken at time t_1 and the following ones separated by a time gap Δt of about 8.3 ms. At time t_1 (purple curve), a primary attachment is observed on the right-hand side of the anode wall, and a second one is

located at around 225 °. When looking at the blue curve (about 8.3 ms later), this attachment moved from 225 ° to about 200 °, as pointed out by the red arrow labeled “1” in Fig. 7. Moreover, and a third arc root, flagged by the asterisk, has appeared on the top of the anode wall. By comparing the blue and green curves, it appears that this arc root has moved to the right-hand side of the anode wall, as pointed out by the red arrow labeled “2”, which ultimately results in a single main attachment on this side at time t_1+2Δt.

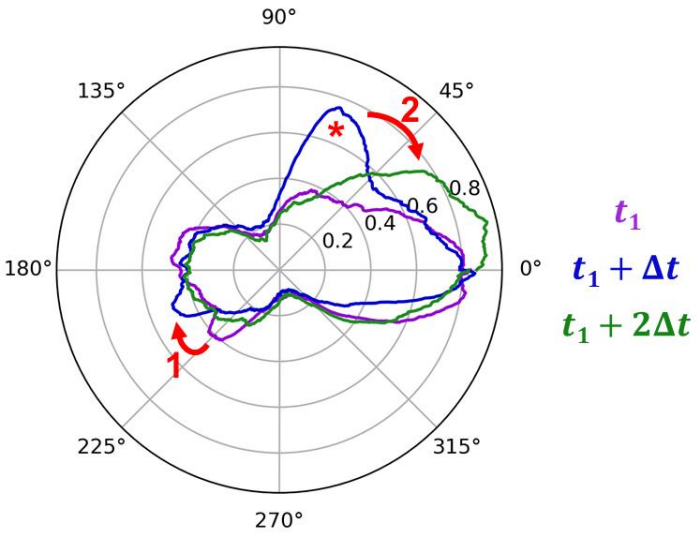

Figure 7: Radar diagram for a succession of three images in the case of the Ar-H_2 mixture with a 9 mm diameter nozzle. Each curve is separated by a time gap Δt of about 8.3 ms, starting with the purple curve, followed by the blue and the green curves.

These findings suggest that anodic arc roots follow a circular movement of weak amplitude when using a 9 mm nozzle. Moreover, a high number of images show a stable anodic arc root observed on the right-hand side of the anode wall, as shown in the example described in Fig. 7 through the analysis of three images. It is however to be noted that this stable arc root was also observed at lower current intensities.

When the nozzle’s diameter is reduced to 6.5 mm (Fig. 6 A2), two arc roots are still visible on the top of the anode wall, and a large bright area is noticeable at the bottom of the nozzle. The plasma light intensity is higher with this reduced diameter as shown by the radar diagram in Fig. 6 A3. It can be assumed that the hot plasma is more uniformly distributed in the nozzle volume, thus higher heat losses are to be expected for reduced nozzle diameters (see further discussion).

The plasma light intensity decreased drastically, as the Ar-He mixture was injected. As a matter of fact, as shown on the radar diagram related to the Ar-He mixture (Fig. 6 B3) and with a 6.5 mm nozzle, a maximum light intensity of about 0.6 a.u. was achieved, in contrast with the 1 a.u. observed with the Ar-H_2 mixture (Fig. 6 A3). As the light intensity was lower for this mixture, particularly with the use of a 9 mm nozzle, it was difficult to clearly identify arc roots with only end-on images. The radar diagram presented in Fig. 6 B3 highlights the presence of three anodic arc roots, pointed out by orange arrows in Fig. 6 B1. Regarding the Ar-H_2 mixture, reducing the nozzle's diameter to 6.5 mm resulted in an increase in light intensity near the anode wall. Moreover, it can be seen in Fig. 6 B2 that anodic attachments were less well-defined than with a 9 mm nozzle, as one large main attachment on the left-hand side of the anode wall is seen, spreading over 40 ° (between 160 ° and 200 ° approximately).

As a partial conclusion, end-on imaging was used to study the influence of the nozzle's diameter on electric arc dynamics and arc attachment for two plasma-forming gas compositions. In the case of the Ar-H_2 mixture with a 9 mm nozzle, a stable anodic arc root was observed and the weak amplitude circular movement of additional well-defined reattachments all around the anode wall was highlighted. For both mixtures, reducing the nozzle from 9 to 6.5 mm resulted in larger bright areas located around the anode wall and in an overall higher plasma light intensity. In order to understand these different behaviors, a visual monitoring of the nozzle was carried out after testing.

Assessments of the anode erosion

A typical SinplexPro™ anode nozzle is made of copper with a lanthanum oxide-doped-tungsten liner. A boron-nitride ring ensures the electrical insulation between the anode nozzle and the neutrodes, while withstanding high temperatures. Figure 8 displays pictures of brand-new nozzles of 9 and 6.5 mm in diameter with their significant parts pointed out.

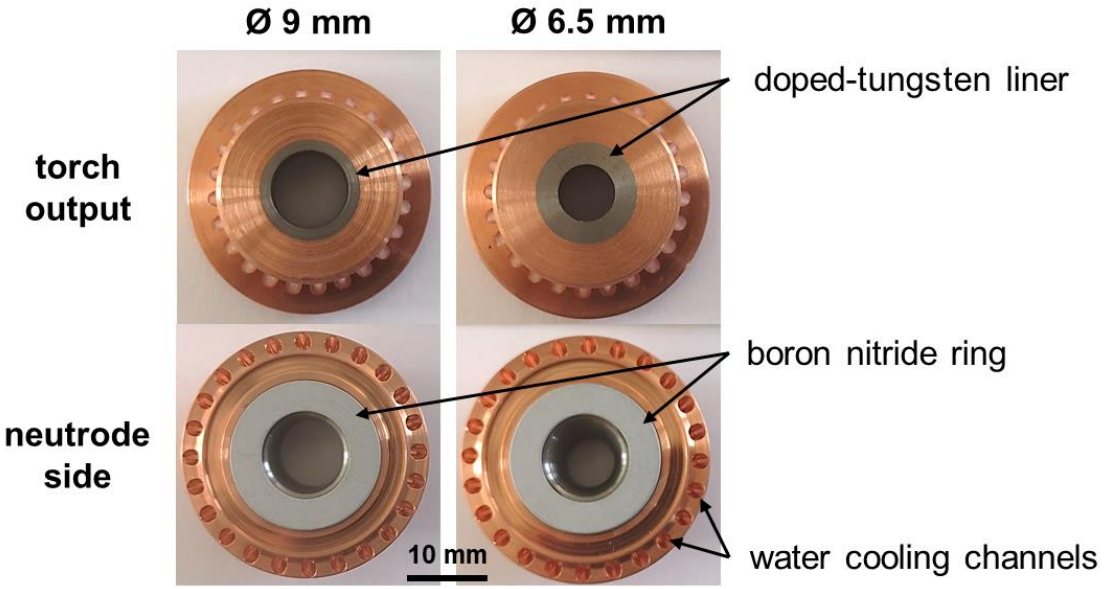

Figure 8: Pictures of brand-new nozzles of 9 and 6.5 mm in diameter.

Figure 9 shows three pictures of the nozzle taken from the neutrode side after testing. It appears that nozzles of both diameters were exposed to both plasma-forming gas compositions and that erosion occurs at the upstream edge of the anode, close to the boron nitride ring, as noticeable on Fig. 9 A and B. In a 9 mm nozzle (Fig. 9 A), the inner surface is smooth, with no signs of erosion, as opposed to the inner surface of the 6.5 mm nozzle, which shows signs of grooves along the anode wall at higher magnification (Fig. 9 C).

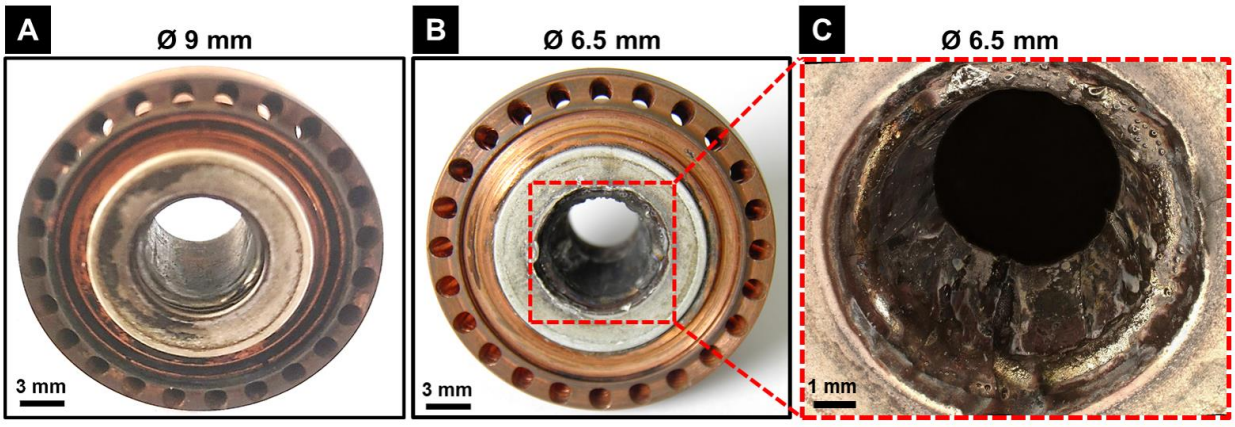

Figure 9: Pictures inside the nozzle after testing of A) a 9 mm diameter nozzle, B) a 6.5 mm diameter nozzle and C) the inner surface of a 6.5 mm diameter nozzle at higher magnification.

The anode erosion illustrates the preferential arc root locations in the arc dynamics which are suspected to be mainly at the upstream edge of the 9 mm nozzle and are extended along the

anode wall for the 6.5 mm diameter nozzle. The examination of the arc voltage signals is relevant to complete the interpretation of the arc motion.

Arc root motion in the anode nozzle

The presence of the noticed grooves in the 6.5 mm nozzle may be explained by studying the current and voltage signals. It is stated that in a 6.5 mm nozzle, there is a longitudinal movement of the arc root resulting in longitudinal erosion. Besides, the movement being slightly circular in the 9 mm nozzle, it might not affect the arc length.

Figure 10 represents the voltage, current and electrical power signals for both types of nozzles subjected to the two mixtures.

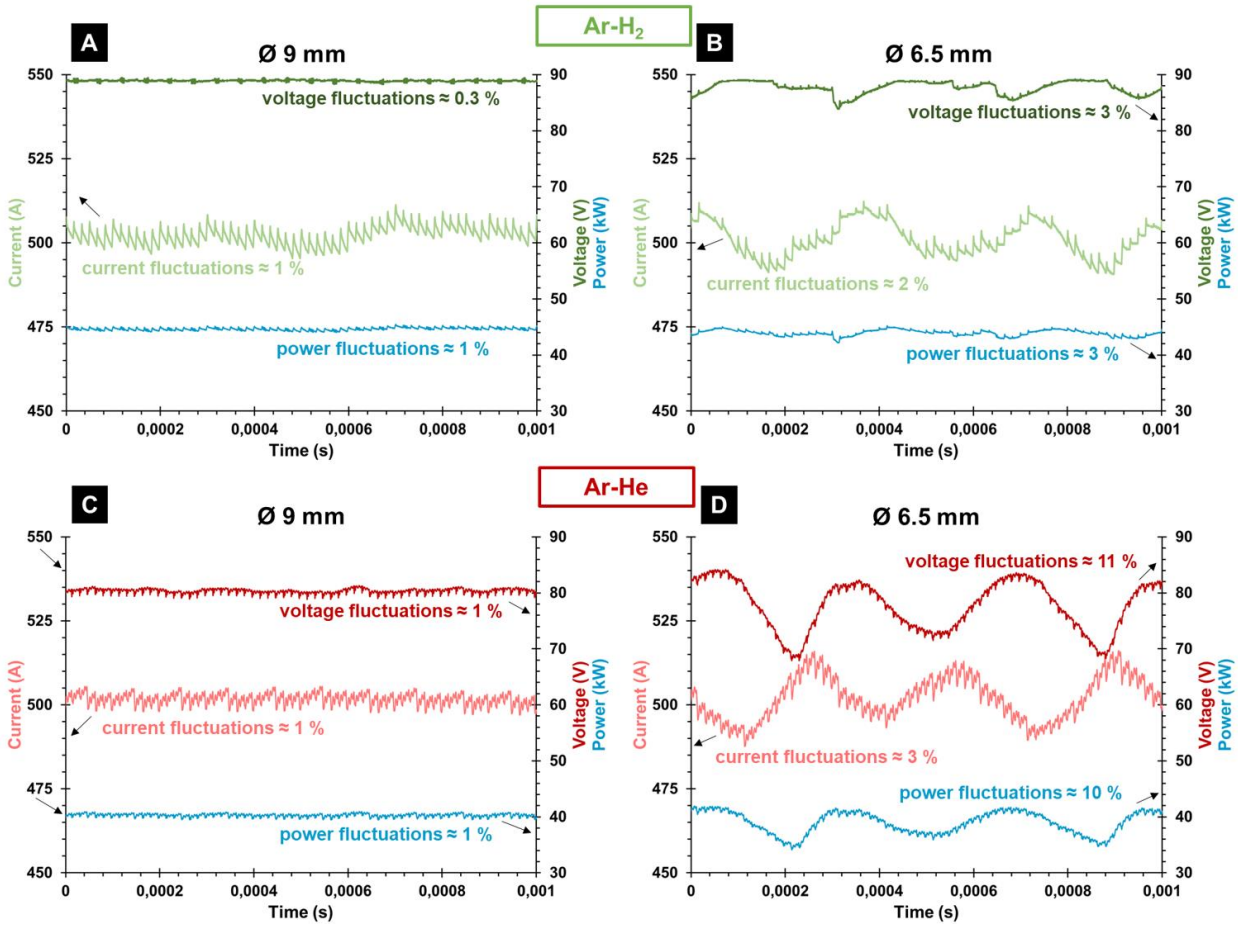

Figure 10: Current, voltage and electrical power signals for the Ar-H_2 mixture with a A) 9 mm nozzle and B) 6.5 mm nozzle, and for the Ar-He mixture with a C) 9 mm nozzle and D) 6.5 mm nozzle. Adapted from (Ref 10).

In Fig. 10 A and C (9 mm nozzle), voltage and current fluctuations are very low (maximum 1 %) especially in the presence of H_2, which is very different from a conventional plasma torch

behavior where the addition of H_2 usually leads to high voltage fluctuations (Ref 20). One may note that the high frequency fluctuation of 60 kHz seen on both current and voltage comes from the power supply regulation. In Fig. 10 B and D (6.5 mm nozzle), larger current and voltage fluctuations (up to 11 % for the Ar-He mixture) were measured at approximately 3 kHz, resulting in power fluctuations of 10 % (Fig.10 D). Table 2 gathers the mean voltage and the voltage fluctuations at 300, 400 and 500 A for both plasma-forming gas compositions and both nozzle diameters, in order to evaluate the influence of the current on the arc's stability. For the Ar-H_2 mixture and both nozzle diameters, increasing the arc current from 300 to 500 A seems to have no effect on the mean voltage or voltage fluctuations. For the Ar-He mixture, an increase in the arc current results in an increase in the mean voltage, from 73 to 77 V for the 6.5 mm nozzle and from 73 to 81 V for the 9 mm nozzle. Moreover, in the case of the same mixture with the 6.5 mm nozzle, a slight increase in the voltage fluctuations is observed with an increasing current value. This could be attributed to the very high plasma gas velocity at 500 A in a smaller nozzle (Table 1), resulting in higher hydrodynamic forces applied to the anodic arc root.

Table 2: Mean voltage and voltage fluctuations at different current intensities for both mixtures and nozzle diameters.

Plasma-forming gas	Nozzle diameter (mm)	Current (A)	Mean voltage (V)	Voltage fluctuations (%)
Ar-H_2	6.5	300	88	4
		400	87	4
		500	88	3
	9	300	89	1
		400	89	1
		500	89	0.3
Ar-He	6.5	300	73	8
		400	75	10
		500	77	11
	9	300	73	1
		400	77	1
		500	81	1

In Fig. 10 B and D, a minimum in the current signal corresponds to a maximum in the voltage signal, though with a slight delay. The origin of this delay is still unknown, but an assumption

can be made about the correlation between I_{min} and U_{max} by primarily considering a longitudinal motion of the arc root. As the gas velocity is higher in a smaller nozzle diameter (Table 1 and (Ref 23)), the anodic arc root may be blown downstream from its initial position, resulting in a longer electric arc and thus a higher arc voltage. Likening the electric arc to a conductive wire, its resistance R can be defined by $R = \frac{\rho L}{S}$, with ρ being the arc resistivity (Ω.m), L its length (m) and S its section (m^2). Assuming that ρ and S remain constant, a longer electric arc would lead to an increase in the electrical resistance. Thus, the current flow will be more difficult, resulting in a lower current intensity as the voltage increases. This time variation of the electrical resistance has been highlighted by the following calculations. Two attachment points of the arc on the nozzle were considered, namely positions 1 and 2 whose arc lengths are L_1 and L_2 and their resistances R_1 and R_2, respectively, as shown on Fig. 11.

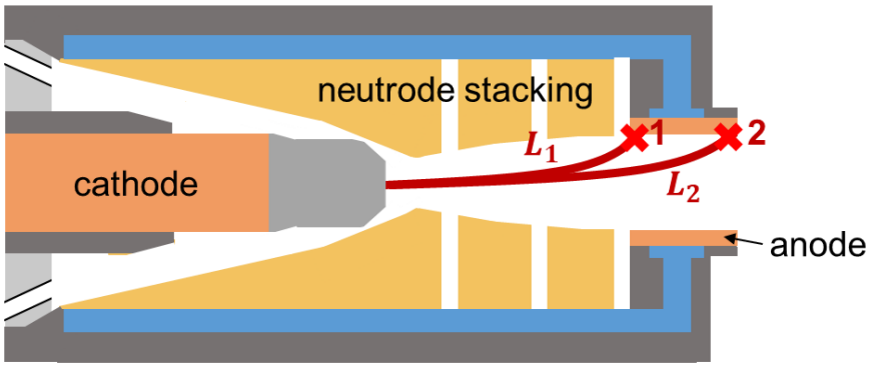

Figure 11: Arc attachment points on the nozzle wall.

Assuming that the resistivity ρ and the cross-section S of the arc remain constant between positions 1 and 2, R_1 and R_2 can be defined as $R_1 = \frac{\rho L_1}{S}$ and $R_2 = \frac{\rho L_2}{S}$. It is then possible to obtain R_2 as follows: $R_2 = \frac{\rho L_2}{S} - \frac{\rho L_1}{S} + \frac{\rho L_1}{S} = \frac{\rho}{S}(L_2 - L_1) + \frac{\rho L_1}{S}$, and thus the resistance ratio $\frac{R_2}{R_1}$ becomes:

$$\frac{R_2}{R_1} = \frac{(L_2 - L_1)}{L_1} + 1 \qquad (4)$$

where the distance $L_2 - L_1$ represents the arc root movement alongside the anode wall. From the voltage and current signals, an electric arc resistance signal $R = f(t)$ may be derived,

leading to the extraction of maximum and minimum values for the resistances. Thus, Equation *(4)* becomes:

$$\frac{R_{max}}{R_{min}} = \frac{(L_{max} - L_{min})}{L_{min}} + 1$$

In this equation, L_{min} can be estimated as to the distance between the cathode tip and the nozzle entrance, which is 26.6 mm as shown in Fig. 1. The term $L_{max} - L_{min}$ is then calculated from Equation *(5)*:

$$L_{max} - L_{min} = \left(\frac{R_{max}}{R_{min}} - 1\right) * L_{min} \quad (5)$$

Table 3 gathers the values obtained for R_{max}, R_{min} and $L_{max} - L_{min}$, corresponding to the arc root movement alongside the anode wall, considering the two mixtures and diameters studied. These results highlight a significant longitudinal movement in the 6.5 mm nozzle. As an example, in the case of the Ar-He mixture with the smaller nozzle, the arc root movement is about 7.5 mm alongside the anode wall, in contrast with the 1.1 mm showed for the 9 mm nozzle.

Table 3: Electric resistance values and arc longitudinal movement for both mixtures and nozzles.

Plasma-forming gas	Nozzle diameter (mm)	R_{max} (Ω)	R_{min} (Ω)	$L_{max} - L_{min}$ (mm)
Ar-H_2	6.5	0.184	0.159	4.3
Ar-He		0.171	0.133	7.5
Ar-H_2	9	0.176	0.169	0.8
Ar-He		0.163	0.156	1.1

Finally, the longitudinal movement of the electric arc alongside the anode wall in a 6.5 mm nozzle, as shown in Fig. 9 C with the presence of grooves, results in a variation of the electrical resistance, whereas arc roots are mainly located at the upstream edge of the nozzle in the case of a 9 mm nozzle.

Therefore, it has been shown that the use of a 6.5 mm nozzle leads to higher voltage fluctuations and to a significant erosion, as mentioned in the section dealing with nozzle monitoring after testing.

The presence of grooves due to the electric arc motion in a 6.5 mm nozzle may lead to different plasma torch thermal balances since it could demonstrate a higher heat diffusion, followed by higher heat losses in smaller nozzles.

Influence on the thermal balance of the plasma torch

As the light intensity measured is higher, end-on imaging suggests that the plasma gas radial temperature distribution (temperature close to the nozzle wall) is higher with a 6.5 mm nozzle than with a 9 mm one. This assumption is supported by the study of thermal balances. Table 4 collects the heat losses, the plasma torch thermal efficiency η, and the specific enthalpy h.

Table 4: Heat losses, thermal efficiency and specific enthalpy for the two mixtures and nozzle diameters.

Plasma-forming gas	Nozzle diameter (mm)	Heat losses (kW)	Thermal efficiency (%)	Specific enthalpy ($MJ.kg^{-1}$)
Ar-H_2	9	21.7	51	15.1
	6.5	26.2	40	11.7
Ar-He	9	11	73	20.1
	6.5	15.5	60	16

It appears that heat losses at the anode wall are higher in a 6.5 mm nozzle and this for both mixtures. As an example, heat losses for the Ar-He mixture rise from 11 to 15.5 kW in the 9 and 6.5 mm nozzles respectively. As in a 6.5 mm nozzle the arc root is moving in a longitudinal way, the nozzle wall is heated over a large area and may require greater cooling than in a 9 mm nozzle, where the arc root is mainly located at the nozzle entrance, as predicted in (Ref 24). As expected, the Ar-H_2 mixture leads to high heat losses (up to 26.2 kW in a 6.5 mm nozzle) due to the H_2 dissociation, resulting in an increase in plasma gas thermal conductivity at 3,500 K (Fig. 12). Conductive losses between the plasma gas and the anode wall are therefore higher, increasing the heat flux at the anode wall. Moreover, a higher thermal gradient is assumed for the Ar-H_2 mixture from end-on images, which leads to higher conductive losses. This phenomenon gives rise to the low thermal efficiency noticed for this mixture (with a maximum of 51 %).

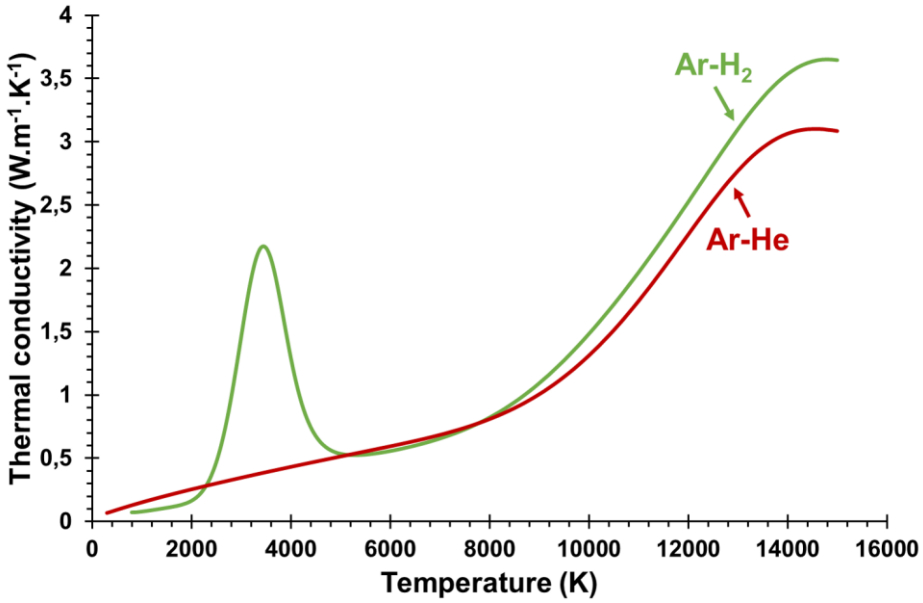

Figure 12: Evolution of the thermal conductivity as a function of the temperature for the Ar-H_2 and Ar-He mixtures. Adapted from (Ref 10).

Comparatively, a high thermal efficiency was recorded for the Ar-He mixture with a 9 mm nozzle (with more than 70 %) and may be explained as follows. As seen in Fig. 6 B1, the plasma light intensity is lower for the Ar-He mixture at the anode wall, meaning that the temperature and probably the thermal gradient as well might be lower for this mixture. It has then to be noticed that the addition of helium to argon results in a shift to higher temperature of the electrical conduction threshold, due to the high ionization energy of helium. The gas electrical conductivity in the cold boundary layer is lower, leading to lower Joule heating. Moreover, Cressault *et al*. (Ref 25) calculated the net emission coefficient for different Ar-He mixtures. When helium is added to argon, the net emission coefficient slightly decreases, thus, radiative losses in the presence of helium are reduced. These two phenomena, associated with a lower thermal conductivity for the Ar-He mixture up until 5,000 K (Fig. 12), may partially explain the high thermal efficiency recorded for this mixture. It then leads to low radial thermal heat flux at the boundary layer with such a larger diameter nozzle.

Furthermore, Table 4 presents the specific enthalpy for the two nozzle diameters. As thermal efficiencies are lower in the 6.5 mm nozzle, lower specific enthalpy values are reached. For

both mixtures, it decreases by 20 % and, for instance in the case of the Ar-He mixture, drops from 20.1 $MJ.kg^{-1}$ to 16 $MJ.kg^{-1}$ with a 9 and 6.5 mm nozzles respectively.

Finally, it has been shown that reducing the nozzle diameter has a strong influence on the electric arc dynamics and thermal balance of the plasma torch. The following subsection investigates the influence of the nozzle diameter on plasma jet stability.

Influence on plasma jet stability at nozzle exit

The low frequency voltage fluctuations observed with a 6.5 mm nozzle directly affect the plasma jet stability. Figure 13 represents the voltage and plasma jet light fluctuations spectra for both mixtures recorded at the nozzle exit. Plasma jet light fluctuations were recorded by following the Ar I line at 420 nm by optical emission spectroscopy, as explained in Fig. 2.

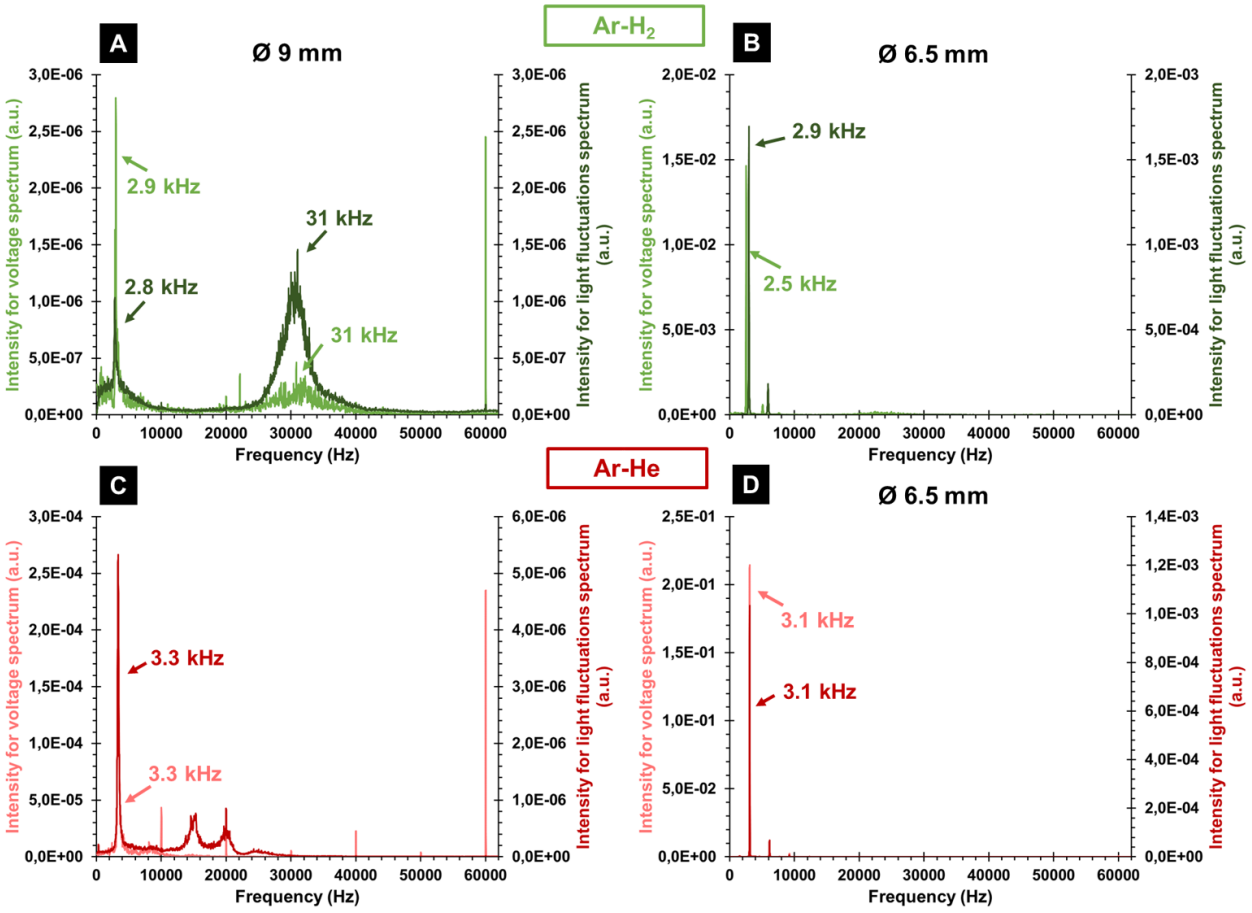

Figure 13: Voltage and plasma jet light fluctuations spectra for the Ar-H_2 mixture in a A) 9 mm nozzle and B) 6.5 mm nozzle and for the Ar-He mixture in a C) 9 mm nozzle and D) 6.5 mm nozzle. Adapted from (Ref 10).

The main voltage fluctuation frequency is ranging from 2.5 to 3.5 kHz for both nozzles and both mixtures. This low frequency fluctuation correlates with the one measured on the plasma jet light fluctuations, which means that it may be attributed to the electric arc movement. In the case of the 9 mm nozzle (Fig. 13 A and C), the peak intensity is very low (being around 10^{-6} and 10^{-4} a.u. for the Ar-H_2 and the Ar-He mixtures, respectively) for both voltage and light fluctuations, thus, the impact on particle treatment should be limited. Regarding the Ar-H_2 mixture, a fluctuation is also found at around 31 kHz on both spectra (Fig. 13 A); it should however not affect the particle treatment either, due to its high frequency occurrence. Moreover, with the 6.5 mm nozzle (Fig. 13 B and D), the peak intensity of the 2.5 – 3.5 kHz range fluctuation is at least three orders of magnitude higher than with the 9 mm nozzle (around 10^{-2} a.u. for the Ar-H_2 mixture and 10^{-1} a.u. for the Ar-He mixture). The in-flight particle characteristics and coating properties for the two nozzle diameters and both mixtures are studied at the end of this section, and shall allow figuring out if the higher fluctuation in a 6.5 mm nozzle affects the coating properties.

Influence of the in-flight particle characteristics and coating properties

The lower specific enthalpy recorded in a 6.5 mm nozzle has a strong influence on in-flight particle characteristics. This is illustrated on Fig. 14, where the particle temperature is represented as a function of the particle velocity for the two nozzles and mixtures of plasma-forming gases at 120 mm from the nozzle exit.

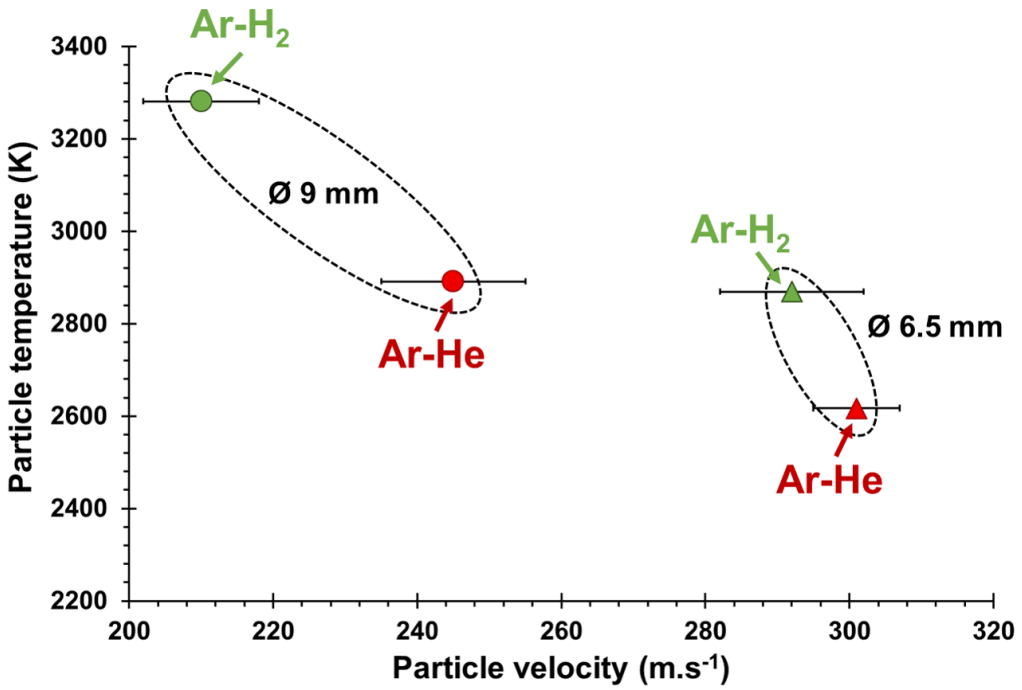

Figure 14: In-flight particle characteristics for a ZrO_2-7wt.%Y_2O_3 powder at 120 mm from the nozzle exit for each experimental condition.

Reducing the nozzle from 9 to 6.5 mm results in a higher particle velocity and a lower particle temperature for both mixtures. For instance, the Ar-He mixture displays a particle velocity of 245 ± 10 $m.s^{-1}$ in the 9 mm nozzle, while it can reach 300 ± 6 $m.s^{-1}$ in the 6.5 mm one.

As the plasma velocity is higher in a 6.5 mm nozzle (Table 1), the residence time of the particles is lower and heat exchanges between the plasma and the particles are less efficient, resulting in a lower particle temperature for both mixtures in a 6.5 mm diameter nozzle.

For a same nozzle diameter, the Ar-H_2 mixture displays a higher particle temperature as the presence of H_2 should improve the heat transfer. Moreover, Table 5 records the particle residence time in the plasma jet for the two plasma-forming gas compositions in a 9 mm nozzle. It was calculated using the particle velocity and the plasma hot zone length. This hot zone length has been determined by means of an alumina rod set as described in (Ref 26); it corresponds to the distance between the torch exit and the rod, at which alumina drops are observed at the end of the latter. According to Table 5, the particle residence time is higher for the Ar-H_2 mixture, allowing for a better thermal treatment.

Table 5: Particle residence time for the two plasma-forming gas compositions in a 9 mm nozzle.

Plasma-forming gas	Nozzle diameter (mm)	Particle residence time (ms)
Ar-H_2	9	0.53
Ar-He		0.35

The addition of helium to argon as primary gas results in a higher particle velocity, which can be explained by the higher specific enthalpy observed in this case (Table 4), possibly leading to a higher plasma temperature and a lower plasma gas density.

These disparities in in-flight particle characteristics directly affect the coating microstructures, as shown in Fig. 15, representing microstructures on a *particle velocity-temperature* mapping.

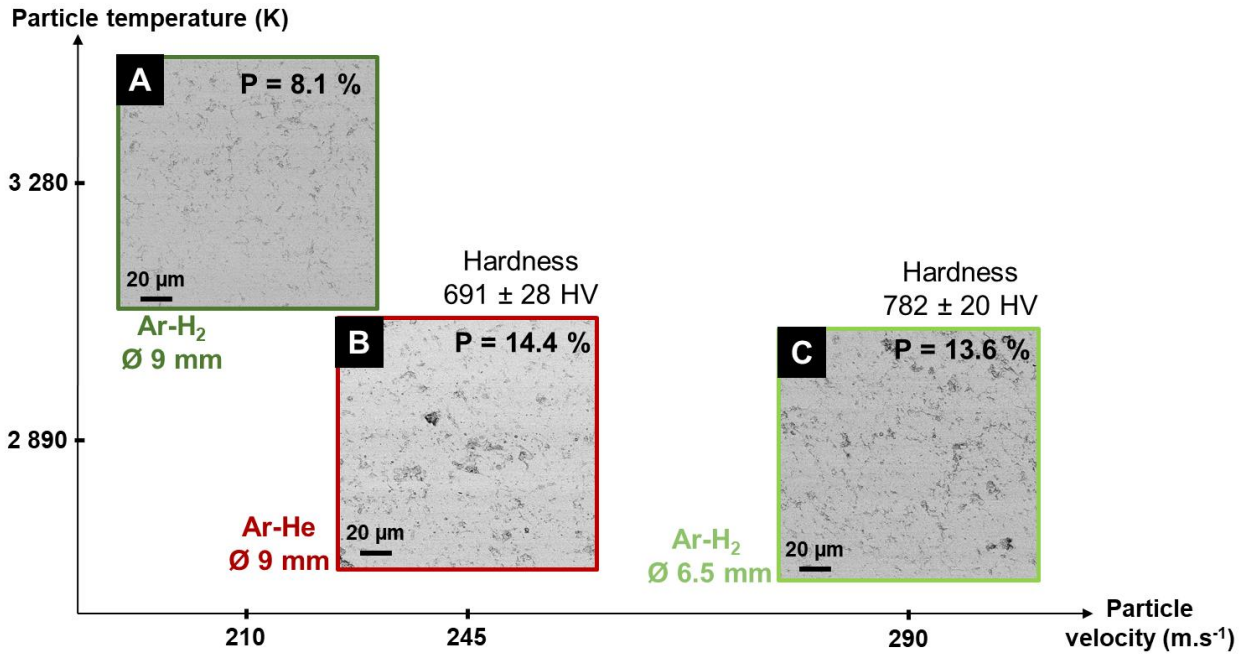

Figure 15: Coating microstructures on a particle velocity-temperature mapping: A) Ar-H_2 mixture in a 9 mm nozzle, B) Ar-He mixture in a 9 mm nozzle and C) Ar-H_2 mixture in a 6.5 mm nozzle.

Firstly, it is to be noted that only three coating microstructures are presented here: Fig. 15 A and C deal with the Ar-H_2 mixture with both nozzles, whereas Fig. 15 B handles the Ar-He mixture with the sole 9 mm nozzle. It was indeed not possible to produce a coating for the Ar-He mixture with the smaller nozzle, probably due to the very low particle temperature. The

deposition rate was only 5 % for this mixture, as compared to about 50 % for the three others conditions (Table 6).

Figure 15 A is a SEM micrograph of the coating microstructure obtained with the 9 mm nozzle and the Ar-H_2 mixture. This experiment leads to a high particle temperature of 3,280 ± 8 K and to a particle velocity of 210 ± 8 $m.s^{-1}$. The coating microstructure presents a low porosity rate of about 8 % (Table 6). The particle temperature decreases to 2,890 K when reducing the nozzle diameter to 6.5 mm, which results in a higher coating porosity (13.6 %).

Considering the same nozzle (9 mm), the particle temperature is lower for the Ar-He mixture (Fig. 15 B) as compared to the Ar-H_2 mixture (Fig. 15 A), which could explain the higher coating porosity for the Ar-He mixture (14.4 %).

Table 6: Deposition rate, coating porosity and coating microhardness for each experimental condition.

Plasma-forming gas	Nozzle diameter (mm)	Deposition rate (%)	Coating porosity (%)
Ar-H_2	9	46	8.1
	6.5	49	13.6
Ar-He	9	49	14.4
	6.5	5	/

The two coatings in Fig. 15 B and C were produced with the two different nozzles and are characterized by a similar coating porosity of about 14 %. It also seems that the higher voltage fluctuations recorded with a 6.5 mm nozzle, identified on the plasma jet light fluctuations as well, have no influence on the coating porosity for the two mixtures. Another point to consider is the cohesion of the coatings. For a same coating porosity, regarding the two coatings on Fig. 15 B and C, the Ar-H_2 mixture displays a higher coating hardness (780 ± 20 HV) than the Ar-He mixture (682 ± 28 HV). This highlights the significance of hydrogen for a better thermal treatment of the particles. Finally, using hydrogen in a 6.5 mm nozzle could be useful in order to control the coating porosity, as shown in Table 6.

Conclusions

The cascaded-anode plasma torch design allows reducing electric arc fluctuations and increasing the mean voltage as compared to conventional plasma torches. In this work, electric arc dynamics were studied for two nozzle diameters (9 and 6.5 mm) used in a cascaded-anode plasma torch for two mixtures (Ar-H_2 and Ar-He). Anodic observations revealed that, in a 9 mm nozzle, the arc attachment was mainly located at the upstream edge of the anode wall, near the boron-nitride ring, as well as that a circular movement of weak amplitude of several arc roots was observed. In a 6.5 mm nozzle, a longitudinal movement of the electric arc was favored along the anode wall, as suggested by the after-testing nozzle monitoring and by the variation in electrical resistance. This electric arc movement in a reduced nozzle diameter could explain the higher voltage fluctuations measured (11 % for the Ar-He mixture as compared to 1 % with a 9 mm nozzle).

Higher heat losses at the wall of the 6.5 mm nozzle suggest a warmer plasma gas more evenly distributed in the nozzle volume with reduced nozzle diameter. This results in higher heat losses at the level of the anode wall. On the other hand, the use of a 9 mm nozzle leads to a higher stability for the electric arc and the plasma jet, lower heat losses at the anode wall, a higher thermal efficiency and lower anode erosion, and this for both mixtures as well.

The Ar-H_2 mixture with a 9 mm nozzle was characterized by the lowest voltage fluctuation percentage (less than 1 %). The high thermal conductivity presented by this mixture probably leads to a warmer plasma gas in the cold boundary layer, which favors arc reattachments occurring in a same vertical plan and could thus explain the low voltage fluctuations.

The Ar-He mixture leads to lower plasma light radiative emissions, resulting in lower heat losses at the level of the anode wall and in a high thermal efficiency.

Reducing the nozzle diameter from 9 to 6.5 mm leads to a higher particle velocity and a lower particle temperature, resulting in a higher coating porosity. It would also seem that the higher voltage fluctuations observed in a 6.5 mm nozzle have no influence on the coatings porosity for the two plasma gas mixtures used in this study. The Ar-H_2 mixture leads to a high particle temperature, resulting in a low coating porosity with the 9 mm nozzle. Finally, it appears that it is possible to use hydrogen in a 6.5 mm nozzle on a Sinplex torch.

Depending on the application desired, an Ar-H_2 mixture may be used in a 6.5 mm nozzle in order to control the porosity of the coating. However, higher erosion was observed in this configuration. A compromise has then to be found in order to limit the anode erosion while using hydrogen in a 6.5 mm nozzle.

References

1. P. Fauchais and M. Vardelle, Plasma Spraying: Present and Future, *Pure Appl. Chem.*, 1994, **66**(6), p 1247–1258.

2. S.A. Wutzke, E. Pfender, and E.R.G. Eckert, Study of Electric Arc Behavior with Superimposed Flow., *Am. Inst. Aeronaut. Astronaut.*, 1967, **5**(4), p 707–714.

3. P. Fauchais and A. Vardelle, Thermal Plasmas, *IEEE Trans. Plasma Sci.*, 1997, **25**(6).

4. Z. Duan and J. Heberlein, Arc Instabilities in a Plasma Spray Torch, *J. Therm. Spray Technol.*, 2002, **11**(1), p 44–51.

5. V. Rat, F. Mavier, and J.F. Coudert, Electric Arc Fluctuations in DC Plasma Spray Torch, *Plasma Chem. Plasma Process.*, 2017, **37**(3), p 549–580.

6. J.F. Coudert, V. Rat, and D. Rigot, Influence of Helmholtz Oscillations on Arc Voltage Fluctuations in a Dc Plasma Spraying Torch, *J. Phys. D: Appl. Phys.*, 2007, **40**(23), p 7357–7366.

7. J.F. Coudert and V. Rat, Influence of Configuration and Operating Conditions on the Electric Arc Instabilities of a Plasma Spray Torch: Role of Acoustic Resonance, *J. Phys. D: Appl. Phys.*, 2008, **41**(20), p 205-208.

8. S. Ghorui, N. Tiwari, K.C. Meher, A. Jan, A. Bhat, and S.N. Sahasrabudhe, Direct Probing of Anode Arc Root Dynamics and Voltage Instability in a Dc Non-Transferred Arc Plasma Jet, *Plasma Sources Sci. Technol.*, 2015, **24**(6), p 065003.

9. J.-L. Marqués, G. Forster, and J. Schein, Multi-Electrode Plasma Torches: Motivation for Development and Current State-of-the-Art, *Open Plasma Phys. J.*, 2009, **2**, p 89–98.

10. C. Ruelle, S. Goutier, V. Rat, A. Keromnes, C. Chazelas, and É. Meillot, Study of the Electric Arc Dynamics in a Cascaded-Anode Plasma Torch, *Surf. Coat. Technol.*, 2023, **462**, p 129493.

11. J.F. Coudert, M.P. Planche, and P. Fauchais, Characterization of d.c. Plasma Torch Voltage Fluctuations, *Plasma Chem. Plasma Process.*, 1995, **16**(S1), p S211–S227.

12. M.P. Planche, J.F. Coudert, and P. Fauchais, Velocity Measurements for Arc Jets Produced by a DC Plasma Spray Torch, *Plasma Chem. Plasma Process.*, 1998, **18**(2), p 263–283.

13. R.C. Seshadri and S. Sampath, Characteristics of Conventional and Cascaded Arc Plasma Spray-Deposited Ceramic under Standard and High-Throughput Conditions, *J. Therm. Spray Technol.*, 2019, **28**(4), p 690–705.

14. G. Darut, M.P. Planche, H. Liao, C. Adam, A. Salito, and M. Rösli, “Study of the In-Flight Characteristics of Particles for Different Configurations of Cascade Plasma Torches,” (Virtual), 2021, p 499–507.

15. X. Cao, D. Yu, and C. Li, Influences of the Arc Chamber Length on the Jet Characteristics of Laminar Plasma Torch, *IEEE Trans. Plasma Sci.*, 2018, **46**(8), p 3017–3021.

16. L. Leblanc and C. Moreau, The Long-Term Stability of Plasma Spraying, *J. Therm. Spray Technol.*, 2002, **11**(3), p 380–386.

17. K. Bobzin, M. Öte, M.A. Knoch, H. Heinemann, S. Zimmermann, and J. Schein, Influence of External Magnetic Fields on the Coatings of a Cascaded Plasma Generator, *IOP Conf. Ser. Mater. Sci. Eng.*, 2019, **480**, p 012004.

18. R. Zhukovskii, C. Chazelas, A. Vardelle, and V. Rat, Control of the Arc Motion in DC Plasma Spray Torch with a Cascaded Anode, *J. Therm. Spray Technol.*, 2020, **29**(1–2), p 3–12.

19. R. Zhukovskii, C. Chazelas, V. Rat, A. Vardelle, and R. Molz, Model of a Non-Transferred Arc Cascaded-Anode Plasma Torch: The Two-Temperature Formulation, *J. Phys. D: Appl. Phys.*, 2022, **55**(6), p 065202.

20. E. Nogues, P. Fauchais, M. Vardelle, and P. Granger, Relation Between the Arc-Root Fluctuations, the Cold Boundary Layer Thickness and the Particle Thermal Treatment, *J. Therm. Spray Technol.*, 2007, **16**(5–6), p 919–926.

21. "National Institute of Standards and Technology," 2022, https://www.nist.gov/pml/atomic-spectroscopy-databases.

22. M.I. Boulos, P. Fauchais, and E. Pfender, "Thermal Plasmas," (Boston, MA), Springer US, 1994.

23. M.P. Planche, "Contribution à l'Étude des Fluctuations dans une Torche à Plasma : Application à la Dynamique de l'Arc et Aux mesure de Vitesse d'Écoulement", ("Study of the Fluctuations in a DC Plasma Torch: Application to the Dynamic Behaviour of the Arc and to the Measurements of the Flow Velocity"), Ph. D. Thesis, University of Limoges, 1995 (in French).

24. R. Zhukovskii, C. Chazelas, V. Rat, A. Vardelle, and R. Molz, Predicted Anode Arc Attachment by LTE (Local Thermodynamic Equilibrium) and 2-T (Two-Temperature) Arc Models in a Cascaded-Anode DC Plasma Spray Torch, *J. Therm. Spray Technol.*, 2022, **31**(1–2), p 28–45.

25. Y. Cressault, M.E. Rouffet, A. Gleizes, and E. Meillot, Net Emission of Ar–H_2 –He Thermal Plasmas at Atmospheric Pressure, *J. Phys. D: Appl. Phys.*, 2010, **43**(33), p 335204.

26. A. Dolmaire, E. Hartikainen, S. Goutier, E. Béchade, M. Vardelle, P.-M. Geffroy, and A. Joulia, Benefits of Hydrogen in a Segmented-Anode Plasma Torch in Suspension Plasma Spraying, *J. Therm. Spray Technol.*, 2021, **30**(1–2), p 236–250.

Figure captions

Figure 1: Schematic with the meaningful dimensions of A) a F4 (conventional plasma torch) and B) a SinplexPro™ (cascaded-anode plasma torch). Adapted from (Ref 10).

Figure 2: Schematic of the different analysis devices used to characterize the SinplexPro™ plasma torch, allowing measuring and recording thermal balances, arc voltage and current fluctuations, anodic arc root motion and plasma jet light fluctuations. Adapted from (Ref 10).

Figure 3: Simulated temperature profile at the nozzle's exit and net emission coefficient profile from (Ref 19) for pure argon at 500 A with a nozzle of 9 mm in diameter.

Figure 4: A) Example of an image obtained with the intensified camera for the Ar-H_2 mixture at 500 A and B) the nozzle's surface and mask delimitations (in orange and yellow respectively), and the line of interest (white) used for image analysis. The camera exposure time is 60 ns.

Figure 5: Schematics of A) the SprayWatch measurements and B) the spraying system.

Figure 6: Examples of end-on images obtained for A1) the Ar-H_2 mixture with a 9 mm diameter nozzle, A2) the Ar-H_2 mixture with a 6.5 mm diameter nozzle, B1) the Ar-He mixture with a 9 mm diameter nozzle and B2) the Ar-He mixture with a 6.5 mm diameter nozzle. Orange and blue arrows point arc roots out. The radar diagrams A3) and B3) correspond to the Ar-H_2 and Ar-He mixtures respectively. The camera exposure is time 60 ns.

Figure 7: Radar diagram for a succession of three images in the case of the Ar-H_2 mixture with a 9 mm diameter nozzle. Each curve is separated by a time gap $\Delta \boldsymbol{t}$ of about 8.3 ms, starting with the purple curve, followed by the blue and the green curves.

Figure 8: Pictures of brand-new nozzles of 9 and 6.5 mm in diameter.

Figure 9: Pictures inside the nozzle after testing of A) a 9 mm diameter nozzle, B) a 6.5 mm diameter nozzle and C) the inner surface of a 6.5 mm diameter nozzle at higher magnification.

Figure 10: Current, voltage and electrical power signals for the Ar-H_2 mixture with a A) 9 mm nozzle and B) 6.5 mm nozzle, and for the Ar-He mixture with a C) 9 mm nozzle and D) 6.5 mm nozzle. Adapted from (Ref 10).

Figure 11: Arc attachment points on the nozzle wall.

Figure 12: Evolution of the thermal conductivity as a function of the temperature for the Ar-H_2 and Ar-He mixtures. Adapted from (Ref 10).

Figure 13: Voltage and plasma jet light fluctuations spectra for the Ar-H_2 mixture in a A) 9 mm nozzle and B) 6.5 mm nozzle and for the Ar-He mixture in a C) 9 mm nozzle and D) 6.5 mm nozzle. Adapted from (Ref 10).

Figure 14: In-flight particle characteristics for a ZrO_2-7wt.%Y_2O_3 powder at 120 mm from the nozzle exit for each experimental condition.

Figure 15: Coating microstructures on a particle velocity-temperature mapping: A) Ar-H_2 mixture in a 9 mm nozzle, B) Ar-He mixture in a 9 mm nozzle and C) Ar-H_2 mixture in a 6.5 mm nozzle.

Tables

Table 7: Experimental conditions implemented, as well as gas velocity and gas residence time for the two nozzle diameters.

Plasma-forming gas	Total mass flow rate ($g.s^{-1}$)	Current (A)	Nozzle diameter (mm)	Gas velocity ($m.s^{-1}$)	Gas residence time (ms)
$Ar-H_2$	1.50	500	9	715	0.017
			6.5	1190	0.010
Ar-He	1.44		9	1355	0.009
			6.5	2290	0.005

Table 8: Mean voltage and voltage fluctuations at different current intensities for both mixtures and nozzle diameters.

Plasma-forming gas	Nozzle diameter (mm)	Current (A)	Mean voltage (V)	Voltage fluctuations (%)
$Ar-H_2$	6.5	300	88	4
		400	87	4
		500	88	3
	9	300	89	1
		400	89	1
		500	89	0.3
Ar-He	6.5	300	73	8
		400	75	10
		500	77	11
	9	300	73	1
		400	77	1
		500	81	1

Table 9: Electric resistance values and arc longitudinal movement for both mixtures and nozzles.

Plasma-forming gas	Nozzle diameter (mm)	R_{max} (Ω)	R_{min} (Ω)	$L_{max} - L_{min}$ (mm)
$Ar-H_2$	6.5	0.184	0.159	4.3
Ar-He		0.171	0.133	7.5
$Ar-H_2$	9	0.176	0.169	0.8
Ar-He		0.163	0.156	1.1

Table 10: Heat losses, thermal efficiency and specific enthalpy for the two mixtures and nozzle diameters.

Plasma-forming gas	Nozzle diameter (mm)	Heat losses (kW)	Thermal efficiency (%)	Specific enthalpy ($MJ.kg^{-1}$)
$Ar-H_2$	9	21.7	51	15.1
	6.5	26.2	40	11.7
Ar-He	9	11	73	20.1
	6.5	15.5	60	16

Table 11: Particle residence time for the two plasma-forming gas compositions in a 9 mm nozzle.

Plasma-forming gas	Nozzle diameter (mm)	Particle residence time (ms)
$Ar-H_2$	9	0.53
Ar-He		0.35

Table 12: Deposition rate, coating porosity and coating microhardness for each experimental condition.

Plasma-forming gas	Nozzle diameter (mm)	Deposition rate (%)	Coating porosity (%)
$Ar-H_2$	9	46	8.1
	6.5	49	13.6
Ar-He	9	49	14.4
	6.5	5	/